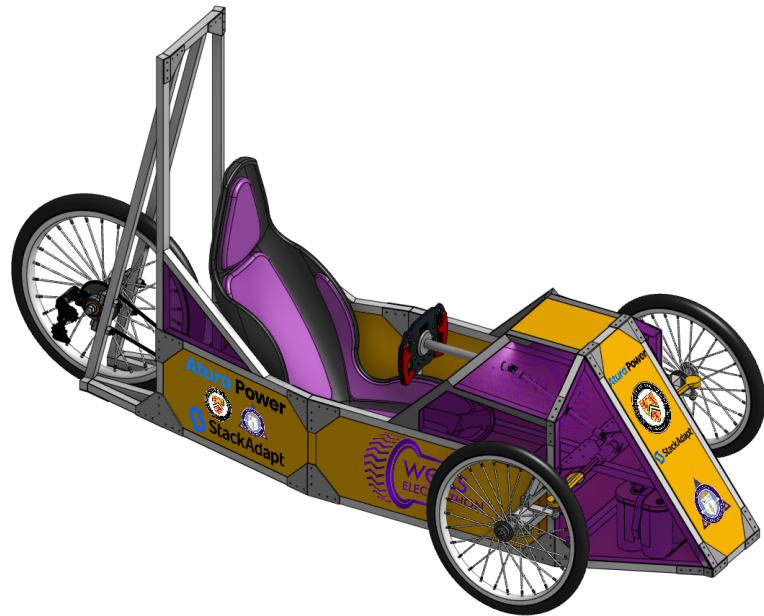


Engineering Design Report

The University of Waterloo EV Challenge 2025

The Warrig X1



White Oaks Secondary School

Zane Beeai, Vidyuth Kripashankar, Ahmad Arab, Angelo Wei

Race Date: May 24, 2025

Contents

1	Introduction	3
1.1	Our Ethos	3
1.2	Design Objectives	3
1.3	Community and Education	4
2	Design Principles	4
2.1	Chassis	4
2.2	Front Drivetrain	4
2.3	Rear Drivetrain	5
2.4	Electrical System	5
3	Frame Design	6
3.1	Material Selection: Aluminum over Steel	6
3.2	Assembly Methodology: Hybrid Joining Strategy	6
3.3	Modularity and Tuning Capabilities	7
3.4	Center of Mass and Load Distribution	7
3.5	Ergonomic Considerations and Driver Comfort	8
4	Front Drivetrain	9
4.1	Spindle Design and Iteration Process	9
4.2	Camber Geometry Justification	11
4.3	Steering Geometry and Kinematics	12
5	Rear Drivetrain	13
5.1	Large Wheel Justification	13
5.2	Motor Selection and Electrical Tradeoffs	13
5.3	Torque and Speed Analysis	14
5.4	Custom Gearbox Design and Implementation	14
5.5	Chain Tensioning and Vibration Mitigation	15
6	Electrical System	17
6.1	Power Architecture: 12V to 24V Conversion	17
6.2	Safety Discharge Subsystem	18
6.3	Telemetry and Sensing System	18
6.4	Thermal Management and Overheating Protection	19
7	Concluding Statements	19
A	Appendix A: CAD Drawings	20
B	Appendix B: Data Tables	22
C	Appendix C: Additional Calculations	24
C.1	Derivation of Linear Acceleration from Torque	24
C.2	Uncertainty in Speed Measurement using a 360 CPR Quadrature/Encoder	24

Acknowledgments

On behalf of the whole WOSS Electrathon Team, we would like to express our gratitude to our mentors and sponsors who have supported us throughout our rookie year:

Mr. Brogly
Mr. Post
Atura Power
Pretium Engineering Inc.
Higginson Equipment Inc.
StackAdapt
The University of Waterloo

1 Introduction

1.1 Our Ethos

Developing the Warrig X1, our first vehicle for the EVC, our team embraced a guiding philosophy of *minimalist engineering*; prioritizing simplicity, functional clarity, and robustness over unnecessary complexity. Each subsystem was scrutinized through the lens of first-principles engineering, supported by simulations, iterative physical testing, and analytical modeling. The result is a maximization of performance and reliability while maintaining a lean, manufacturable design.

Our approach focused heavily on **engineering analysis**: rather than overdesigning or arbitrarily iterating, we used quantitative methods to define requirements, optimize systems, and validate choices. From drivetrain gearing to battery discharge calculations, from torque requirement estimations to dynamic force modeling, we aimed to justify every decision with data and reasoning. Where appropriate, we supplemented this with key engineering principles—such as manufacturability and maintainability—and optimization practices like iterative CAD prototyping and field testing.

This report is structured by subsystem, each framed around engineering problems we encountered and solved. Across the *chassis*, *front and rear drivetrains*, and *electrical system*, we provide a clear account of how we evaluated options, applied mathematical modeling, and performed practical testing to arrive at optimal solutions. While simplicity drove our ethos, rigor drove our decisions.

Our ultimate goal was not to chase a hypothetical ideal, but to build a real, race-ready machine: engineered to perform, engineered to last, and engineered to teach.

1.2 Design Objectives

The following engineering objectives further defined our work:

- **Objective: Prioritize Simplicity Across All Subsystems**

Justification: Simplicity enhances maintainability, reduces failure points, and supports reliable performance during a 70-minute endurance race. It also enables greater accessibility for new team members and simplifies documentation and iteration.

- **Objective: Prioritize DFMA to allow for use of in-House Manual Tools**

Justification: Our school workshop lacks CNC machinery. All parts must be manufacturable using manual mills, lathes, band saws, and hand tools. This constraint encourages precision in design tolerances and realistic CAD modeling that aligns with our fabrication capabilities.

- **Objective: Design for Modularity Across All Subsystems**

Justification: Modular components allow rapid testing and replacement. For example, swapable spindle blocks and a removable, custom gearbox enabled iterative optimization throughout testing without overhauling the entire frame or drivetrain.

- **Objective: Numerically Justify Structural and Mechanical Designs**

Justification: Finite Element Analysis (FEA), free-body diagrams, drivetrain, electrical and more calculations were used to validate that each subsystem could withstand expected loads and race conditions. Quantifiable design verification ensures performance in race conditions.

- **Objective: Integrate Redundancy and Monitoring in the Electrical System**

Justification: Although simplicity is emphasized overall, the electrical system includes controlled startup, voltage discharge safeguards, and basic telemetry sensors (voltage, current, RPM, throttle) to detect anomalies and prevent system failure mid-race.

1.3 Community and Education

While performance and reliability defined our engineering goals, community impact remained central to our purpose. As a team composed primarily of IB students—a curriculum with limited access to technical education—this competition serves as one of our only opportunities to gain real-world engineering experience. In addition, we host weekly workshops every Thursday, welcoming students from across our school, including special education students in the CPP (Community Pathways Program) stream. These sessions have introduced over 30 students to CAD, basic manufacturing, electronics, and programming through hands-on, project-based learning. We strongly believe that the best way to learn engineering is by building together.

2 Design Principles

Our designs are rooted in simplicity, modularity, and robust engineering analysis. Each subsystem was guided by principles that balanced feasibility, manufacturability, and functional performance.

2.1 Chassis

The chassis was designed around the principle of accessible manufacturing. Rather than opting for welded tubular frames, we adopted a gusseted aluminum extrusion chassis, allowing students to fabricate the structure using only standard shop tools. This minimized reliance on specialized equipment while maintaining structural integrity. Weight distribution and rigidity were verified through simulation and testing.



Figure 1: Bare vehicle frame of Warrig.

2.2 Front Drivetrain

To preserve geometric consistency and reduce misalignment, spindle blocks were to be manufactured as unified structures. The suspension itself was designed to be rigid using a principles of torsion and deflection.

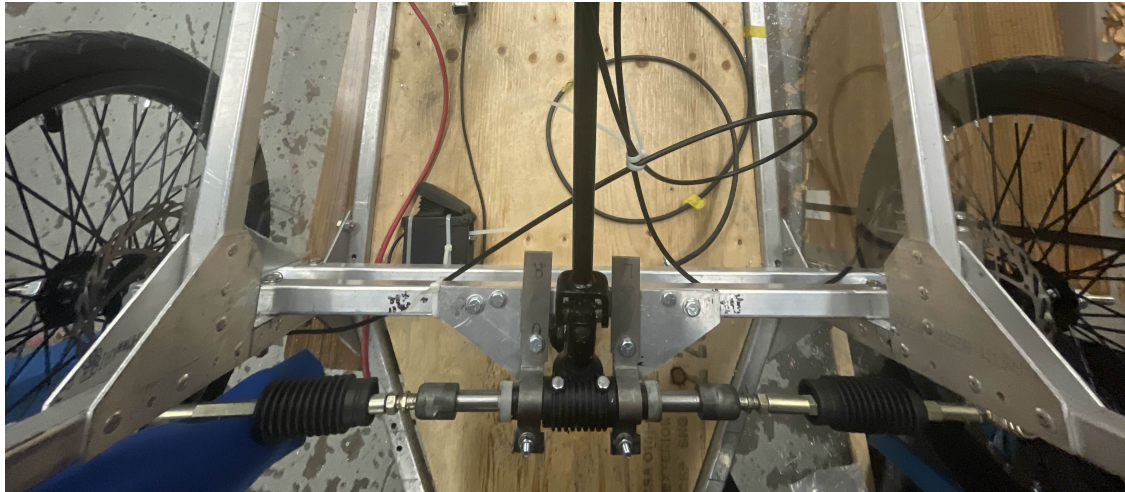


Figure 2: Front drivetrain overhead shot.

2.3 Rear Drivetrain

A larger rear wheel was selected to reduce the necessary gear reduction ratio, thereby improving transmission efficiency. Several motor options were analyzed in-depth, balancing torque output, efficiency curves, and electrical constraints imposed by the boost converter. Drivetrain stability was iterated heavily to ensure minimal loss of efficiency.



Figure 3: Rear drivetrain, without tensioner/idler.

2.4 Electrical System

While much of the vehicle adheres to the ethos of simplicity, the electrical system introduces calculated complexity to ensure operational stability. Most notably, the 12V battery is stepped up to 24V for noticeable improvements in motor efficiency and performance. Other circuits were designed for reliable operation and data collection through integrated telemetry including wheel encoders, satellite-based velocity, and voltage/current monitoring, all of which are treated with known uncertainty margins. Electrical modularity enables quick controller swaps and future upgrades.

3 Frame Design

The design of the frame represents the foundation of our vehicle's structural and ergonomic performance. Adhering to our design ethos of simplicity and engineering rigor, each material and geometric decision was both strategically planned and validated through simulation and analysis.

3.1 Material Selection: Aluminum over Steel

One of the first and most consequential choices in our design process was the selection of aluminum over steel for the primary frame material. Aluminum's significantly lower density (2.7 g/cm^3 [1] compared to 7.85 g/cm^3 for steel [2]) resulted in a substantial reduction in frame weight, as confirmed through CAD-based mass estimates. Finite Element Analysis (FEA) comparisons of identical frame geometries constructed with each material demonstrated a reduction of approximately 74% in mass with the aluminum option, while preserving safety-critical stress tolerances under standard loading conditions. These simulations were validated across multiple scenarios, including frontal impact, cornering torsion, and vertical compression replicating rider weight.



Figure 4: FEA of a frame iteration under 10,000 N of force; over 10 times the conditions in the race, yielding minimal deformation.

3.2 Assembly Methodology: Hybrid Joining Strategy

To balance manufacturability with structural resilience, our frame employed a hybrid joining strategy. Structural gussets were the dominant method of connection, with rivets and bolts selected based on directional loading. Rivets provided superior resistance to shear loads along the plane of the gusset, while bolts were reserved for joints requiring tensile strength and ease of disassembly. The FEA also indicated certain corners where stress accumulated, where we added additional gusseting and welding for strength. TIG welding was selectively used at critical junctions—particularly at the base of the front and rear towers—where multi-axis loading and frequent vibration necessitated continuous metallic bonding. This selective welding approach minimized thermal warping while reinforcing high-stress areas.

3.3 Modularity and Tuning Capabilities

In acknowledgment of our limited access to the official competition track, our design incorporated built-in modularity to support multiple track conditions. The front and rear wheel mounting points support two vertical clearance settings: 1.25" and 2.25". These options allow us to quickly adjust the ride height to accommodate potential surface roughness and lower the center of gravity for better handling if possible. This feature also enabled controlled A/B testing during our field trials.

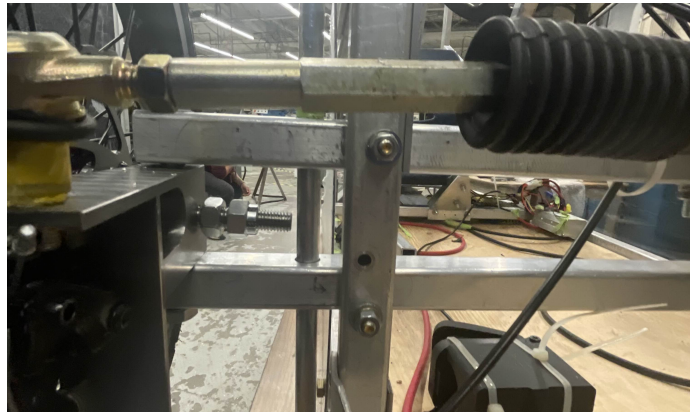


Figure 5: Two discrete clearance settings for the front drivetrain subsystem mounting.

3.4 Center of Mass and Load Distribution

Strategic placement of major mass components yielded a near-even weight distribution along the longitudinal axis. The battery pack was front-mounted to counterbalance the rear motor mass, while the driver mass was centered at the midpoint of the frame. FEA conducted on the central spars confirmed minimal deflection under these loading conditions, with the wider center geometry reinforcing vertical stability. The tapering of the frame toward the rear also improved support for the single rear wheel and enhanced cornering performance by reducing rear track width.

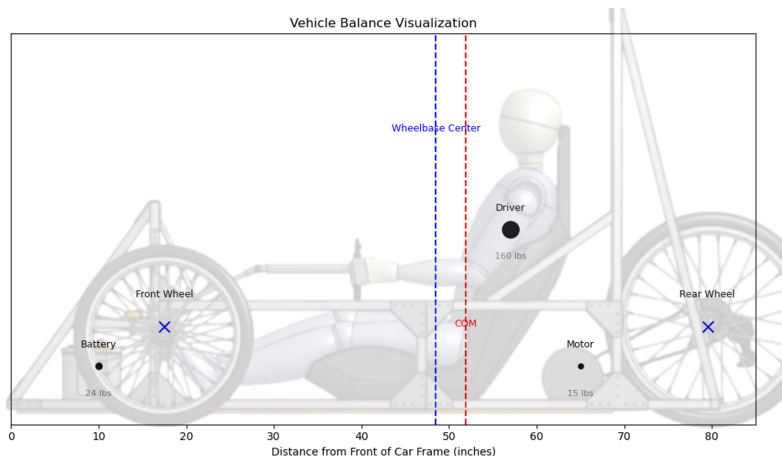


Figure 6: Longitudinal weight distribution graph; slightly back-heavy by design to maintain acceleration while improving steering stability with centered COM relative to the wheelbase.

Under normal race conditions, where the frame experiences a peak strain of $\varepsilon = 3.784 \times 10^{-4}$, the stress in the aluminum structure remains well within the elastic region. Using a Young's modulus of $E = 70$ GPa for 1060 aluminum [3], this corresponds to a stress of approximately 26.5 MPa. This is comfortably below the yield strength range for common tempers such as H12–H14 (60–80 MPa) [4].

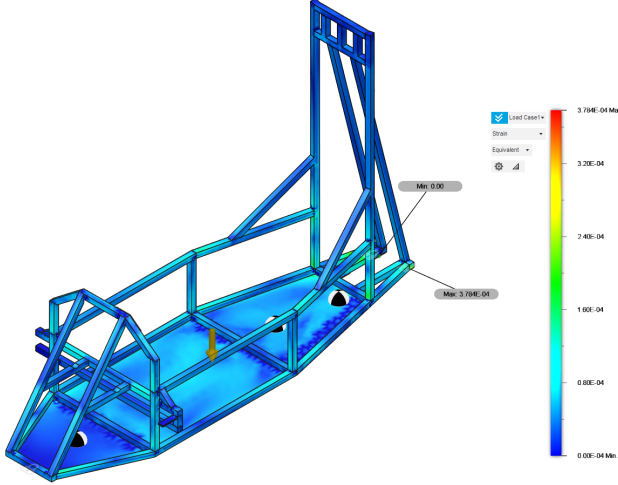


Figure 7: FEA simulation on recent frame iteration with real weight distribution; no visible deformation and minimal Von Mises stress. Little to no stress on spindles and rear wheel mounting bars by design, to alleviate from inevitable forces of steering/load.

To test structural robustness, the extreme loading scenario of 10,000 N was simulated, producing a maximum strain of $\varepsilon = 0.004$ (See Fig. 4). This maps to a stress of approximately 140 MPa on the stress–strain curve for 1060 aluminum [5], approaching or slightly exceeding the yield point for fully hardened H19 temper (140–150 MPa). This indicates that while plastic deformation may occur under extreme, non-race conditions, the frame operates strictly within the elastic regime during all standard race conditions.

This conclusion is visually supported by the stress–strain behavior of 1060 aluminum shown below in Fig. 8, where the evaluated FEA strain points have been overlaid to illustrate their relative position within the material's elastic and plastic regions. The race load condition lies deep within the linear elastic portion of the curve, while the extreme 10,000 N case approaches the onset of yielding, providing a clear graphical validation of the material's performance envelope under both standard and worst-case scenarios.

3.5 Ergonomic Considerations and Driver Comfort

Extended race durations posed the risk of muscle fatigue for drivers [6]. As such, the cockpit geometry was defined with a focus on long-duration ergonomics. CAD simulations and physical mockups confirmed that the footwell provided sufficient extension for a 6'1" driver, and arm space was allocated for comfortable steering and throttle operation. This prevented strain across the shoulders and knees, which is critical for maintaining drivers' attentiveness during the full race duration.

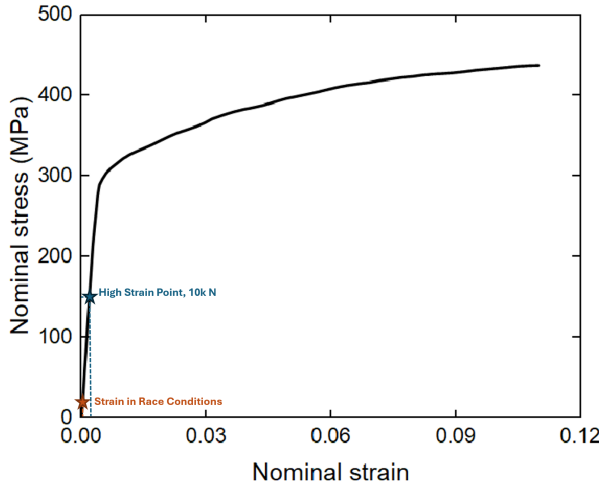


Figure 8: Stress–strain curve of 1060 aluminum with highlighted strain points from FEA simulations. Elastic behavior is maintained under race loads.

4 Front Drivetrain

A core philosophy of our front drivetrain design was ensuring reliability and mechanical simplicity through careful material and geometric selection. Recognizing the spindle as one of the most common points of mechanical failure in electric competition vehicles, we sought to remove as many interfaces as possible. The final spindle assembly was machined as a single continuous block from 1045 steel, minimizing points of failure from multiple components joined in a high-load area. This decision resulted in not only structural simplicity but also geometric precision.

4.1 Spindle Design and Iteration Process

Our initial prototype was milled and TIG-welded in-house from aluminum. While functionally correct, it exhibited significant deflection and material stress during preliminary brake testing, primarily due to misalignment with the disc brake and the lack of FEA-informed reinforcement.

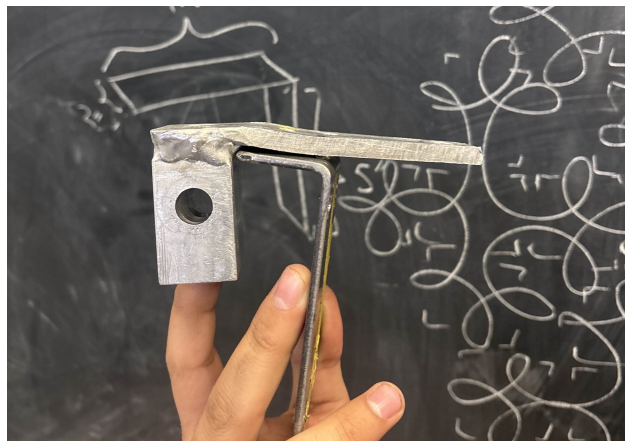


Figure 9: Significant deflection on the aluminum spindle prototype after testing

Brake Force Estimation

To validate spindles' strength under maximum braking load, we calculated the torque and force experienced during worst-case hard stop from 40 km/h within 1.5 seconds using rotational dynamics.

$$v = 40 \text{ km/h} = \frac{40 \times 1000}{3600} = 11.11 \text{ m/s}$$

$$t = 1.5 \text{ s}, \quad m = 100 \text{ kg}, \quad r = 0.254 \text{ m}, \quad f = 0.7$$

$$F_{\text{wheel}} = \frac{f \cdot m \cdot v}{2t} = \frac{0.7 \cdot 100 \cdot 11.11}{2 \cdot 1.5} = 259.23 \text{ N}$$

$$\tau_{\text{spindle}} = F_{\text{wheel}} \cdot r = 259.23 \cdot 0.254 = 65.83 \text{ Nm}$$

Here, we assume an effective load of 100 kg over each front spindle, a 70% efficiency from the brake pads contacting, and calculate a deceleration of $\sim 7.41 \text{ m/s}^2$, indicating an aggressive but non-locking brake scenario at our max velocity of 40 km/h. This braking torque was then used in our FEA simulation to ensure our 1045 steel spindle design could comfortably withstand the stress induced, especially in the asymmetric caliper case modeled at realistic offsets.

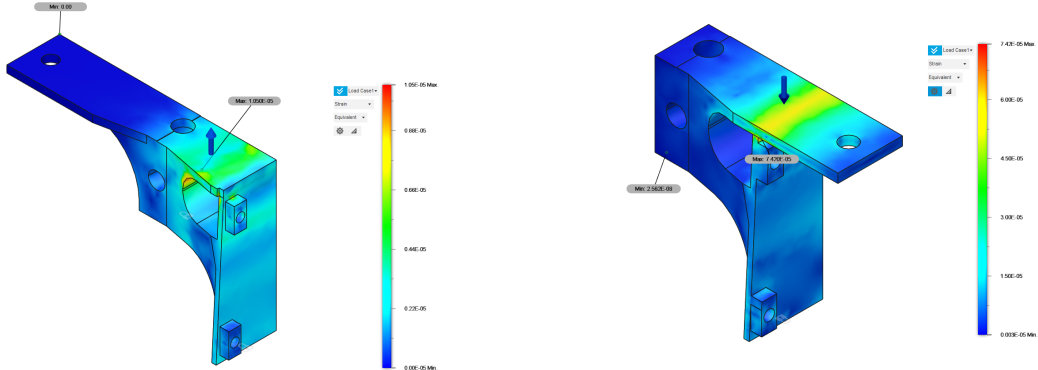


Figure 10: FEA on left and right spindle blocks under maximum braking pressure; no visible deflection and some stress.

FEA simulations of the newly machined AISI 1045 steel spindle blocks under braking loads yielded a maximum strain of 1.05×10^{-5} on the left spindle and 7.42×10^{-5} on the right—differences explained by asymmetric brake geometry. Using the experimentally determined Young's modulus of 223 GPa for normalized 1045 steel [7], these values reflect minimal elastic deformation and confirm improved performance over the previous aluminum prototypes. To estimate how the same geometry would behave if manufactured from 1060 aluminum, we scale the strain using the ratio of elastic moduli:

$$\varepsilon_{\text{Al}} = \varepsilon_{\text{Steel}} \times \frac{E_{\text{Steel}}}{E_{\text{Al}}}, \quad E_{\text{Steel}} = 223 \text{ GPa}, \quad E_{\text{Al}} = 70 \text{ GPa} \implies \frac{E_{\text{Steel}}}{E_{\text{Al}}} \approx 3.19$$

We obtain the estimated strains for aluminum:

$$\varepsilon_{\text{Al, left}} \approx 1.05 \times 10^{-5} \times 3.19 = 3.35 \times 10^{-5}, \quad \varepsilon_{\text{Al, right}} \approx 7.42 \times 10^{-5} \times 3.19 = 2.37 \times 10^{-4}$$

This confirms that equivalent spindle blocks made from 1060 aluminum would deform approximately three times more under the same load (27). These increased strains could compromise spindle alignment and long-term reliability, reinforcing the decision to switch to 1045 steel.

4.2 Camber Geometry Justification

To optimize stability and cornering performance, a negative camber angle of -3° was applied to both front wheels. This choice was not arbitrary; it reflects a balance between maximizing lateral grip and minimizing tire wear losses at our target speeds and track conditions.

The lateral force [8] a tire generates during cornering, denoted F_y , is influenced by both slip angle α and camber angle γ . For small angles and under steady-state cornering, the lateral force can be modeled as:

$$F_y = C_\alpha \cdot \alpha + C_\gamma \cdot \gamma \quad (1)$$

where C_α is the cornering stiffness and C_γ is the camber stiffness. This linearized model is derived from the widely adopted **Pacejka Magic Formula**, developed by Hans B. Pacejka, which models tire dynamics based on empirical behavior [9].

To visualize the camber effect in isolation, for our purposes we refer to the simplified sinusoidal form of the camber-lateral force relationship:

$$F_y(\gamma) = F_{y,\max} \cdot \sin\left(\frac{\pi(\gamma + \gamma_0)}{2 \cdot \gamma_{\text{peak}}}\right) \quad (2)$$

In this equation:

- $F_{y,\max}$ is the maximum achievable lateral force,
- γ is the camber angle in radians,
- γ_{peak} is the camber angle where peak grip occurs (typically $\gamma_{\text{peak}} \approx -3^\circ$),
- γ_0 is an optional offset (set to 0 for symmetric response).

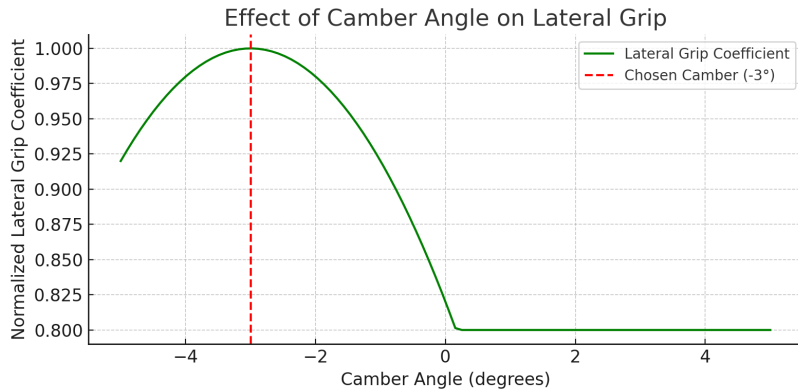


Figure 11: Lateral force vs. camber angle, normalized for peak force. Max grip occurs around -3° .

This plot (Figure 11) confirms that lateral grip increases with negative camber, peaking around -3° , beyond which grip deteriorates due to contact patch distortion and load imbalance.

Given our vehicle's weight distribution, tire type, and turn radii, simulation and modeling showed that -3° provided optimal lateral force characteristics, enhancing cornering predictability without inducing excessive inner-edge wear or scrubbing loss during cornering. This was validated through track testing and subjective steering feel.



Figure 12: Front view of car on test drive, 3° camber is evident.

4.3 Steering Geometry and Kinematics

To ensure optimal maneuverability on the closed-circuit track, the steering system was designed for a theoretical turning radius of 2.50 m, derived from geometric projections over the tightest turns mapped using satellite imagery of the competition venue. The actual measured radius post-build was **2.45 m**, validating the accuracy of our CAD steering angle calculations and physical implementation. Ackermann steering geometry [10] was implemented with an inside wheel maximum angle of 43° and outside wheel angle of 32° at full lock, matching theoretical predictions.

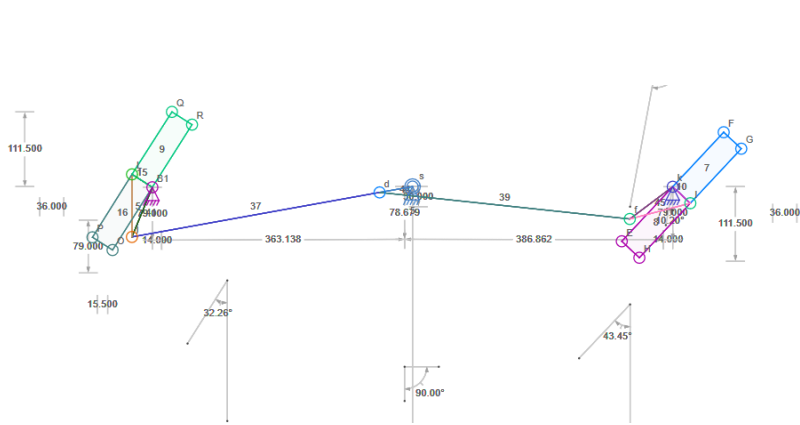


Figure 13: Steering diagram calculated for front drivetrain tuned to 2.5m turn radius (left), image of drive test where Ackerman steering geometry is evident, and a 2.45m actual steering radius was measured (right).

5 Rear Drivetrain

5.1 Large Wheel Justification

A 24-inch rear wheel was selected deliberately as part of a systems-level strategy to improve drivetrain efficiency. Larger wheels require higher torque at a given acceleration but allow for lower RPMs to achieve a desired ground speed. This has two primary advantages:

- **Reduced Reduction Ratio:** For a target top speed of 45–50 km/h, the wheel must rotate between 367–408 RPM. With a high-speed motor like the AmpFlow E30-400-24 operating around 5300 RPM, this corresponds to a required reduction ratio between 13 and 15 without loss. A larger wheel allows this ratio to be achieved with smaller driven sprockets, minimizing chain wrap angles and friction losses in sprockets.
- **Increased Mechanical Advantage at Cruise Speed:** A larger circumference reduces rolling resistance per unit rotation and supports smoother road interaction, lowering vibration and wear during long-duration operation. There is also an increased rolling inertia, which supports cruising.
- **Lowered Tire Wear:** Covering more distance per rotation allows for less tire friction over time, therefore decreasing tire wear and the likelihood of popping a tire.

5.2 Motor Selection and Electrical Tradeoffs

To meet our performance and endurance targets within a limited energy budget (12V, 55Ah), we designed our electrical system around a high-efficiency 24V powertrain supplied by a 20A-limited boost converter at 95% efficiency. This results in a maximum allowable motor input power of:

$$P_{\text{in}} = 24 \text{ V} \times 20 \text{ A} = 480 \text{ W}$$

After evaluating multiple motor options, we found that the widely used ME0909 motor suffered from low efficiency at 12V (as low as 45%), making it unsuitable for our endurance targets. Our solution was to run all motors at 24V, significantly improving their operational efficiency. This choice was validated by motor efficiency curves showing large increases in performance at higher voltage for the same torque range.

Motor Comparison:

- **BY1016Z [11]:** Initial tests were performed using the BY1016Z motor, advertised as 250W and operating at 24V. However, closer inspection of its motor curve revealed that the published torque data referred to internal (pre-reduction) values. After real-world testing, the motor failed to deliver adequate torque, particularly under incline or acceleration loads (26).
- **AmpFlow E30-400-24 [12]:** This motor provided significantly better performance per unit input power. Its peak feasible efficiency under our current-limited boost configuration was found to be 77.8% at 0.667 Nm and 5340 RPM, yielding:

$$P_{\text{out}} = 480 \times 0.778 \approx 373 \text{ W}$$

This formed the basis of our drivetrain calculations (14).

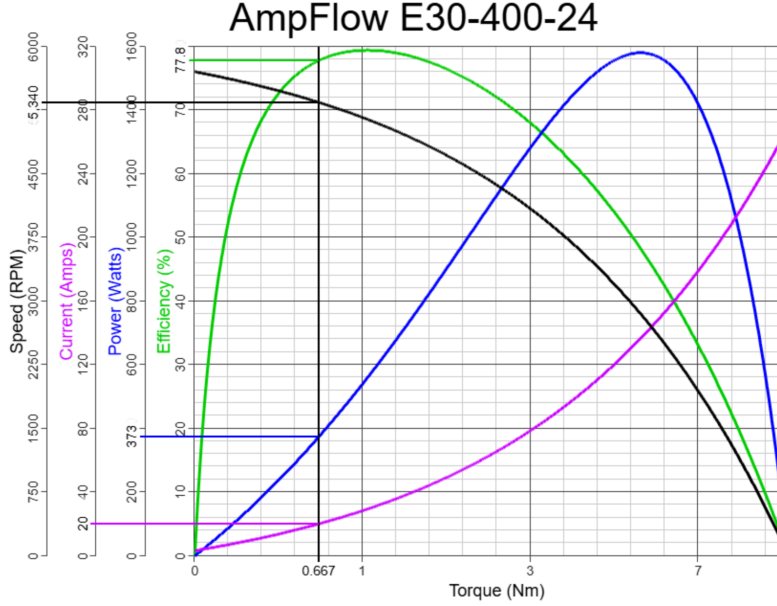


Figure 14: Motor characteristic curve for E30-400-24, point at 20A ($P_{in} = 480\text{ W}$, $P_{out} = 373\text{ W}$).

5.3 Torque and Speed Analysis

For the selected motor, we calculated the required reduction ratios and resulting wheel torque across a range of target top speeds. These values are based on a 24-inch wheel (0.305 m radius):

Speed (km/h)	Wheel RPM	Gear Ratio	Wheel Torque (Nm)	Accel (m/s ²)
35	285	18.74	12.51	0.41
40	325	16.43	10.95	0.36
45	366	14.59	9.73	0.32
50	407	13.12	8.76	0.29

Table 1: Estimated top speeds and accelerations based on motor power output, $a = \frac{2\pi}{dm}$ (C.1)

We targeted a final top speed of 47 km/h, corresponding to a calculated gear ratio of approximately 13.6 and a wheel torque of 9.37 Nm. This ratio ensured acceptable acceleration while delivering a cruise speed close to 40 km/h in real-world conditions, after mechanical losses.

5.4 Custom Gearbox Design and Implementation

To efficiently realize the required reduction, we fabricated a custom gearbox achieving an internal reduction of $81 : 16 \approx 5.06 : 1$. This allowed us to avoid large, inefficient sprockets that would have introduced friction and energy losses. The gears were steel-bushed and mounted to a precision hand-milled steel enclosure, with bearing-supported axles and removable faces for service access. Detailed drawings are provided in Figure 22 in Appendix A. The remaining reduction was implemented using a chain drive with a 55 : 25 ratio. Combining both reductions gave a total of:

$$\text{Total Ratio} = \frac{81}{16} \times \frac{55}{25} \approx 11.1$$

A slight undershoot compromising for lack of parts to create the exact target ratio. This

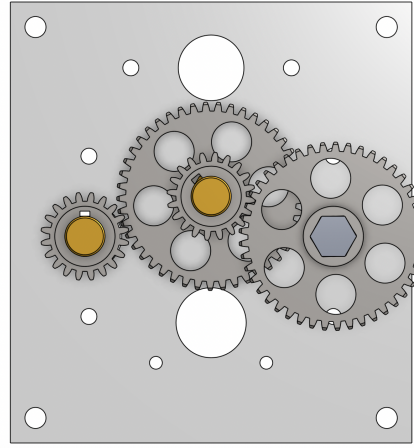


Figure 15: Custom milled 81:16 reduction gearbox CAD file.

resulted in a simulated top speed of ~ 47 km/h after accounting for efficiency, with real-world GPS telemetry confirming a maximum speed of 39.3 km/h and cruising at 25-33 km/h.

5.5 Chain Tensioning and Vibration Mitigation

After two initial extended trials, during which speed and acceleration of the car were progressively increased, it was found that the chain between the rear wheel's sprocket and gearbox sprocket underwent increasingly significant vibrational motion, leading to the chain derailing (see Figure 16). We attributed this recurring problem to two factors: firstly, the light weight of the chain used meant that the constant force exerted by the motor and gearbox created increasingly eccentric rotation of the chain and eventual derailment; secondly, the motor placement was manually achieved, meaning that the chain initially had a leeway distance of ± 1 cm, which created the derailment threshold in the first place. The latter factor was planned in order to preserve the chain's integrity (a chain perfectly tightened along a single axis typically leads to excessive pressure that can compress and break links [13]) but the resultant deviation from these two factors exacerbated each other.

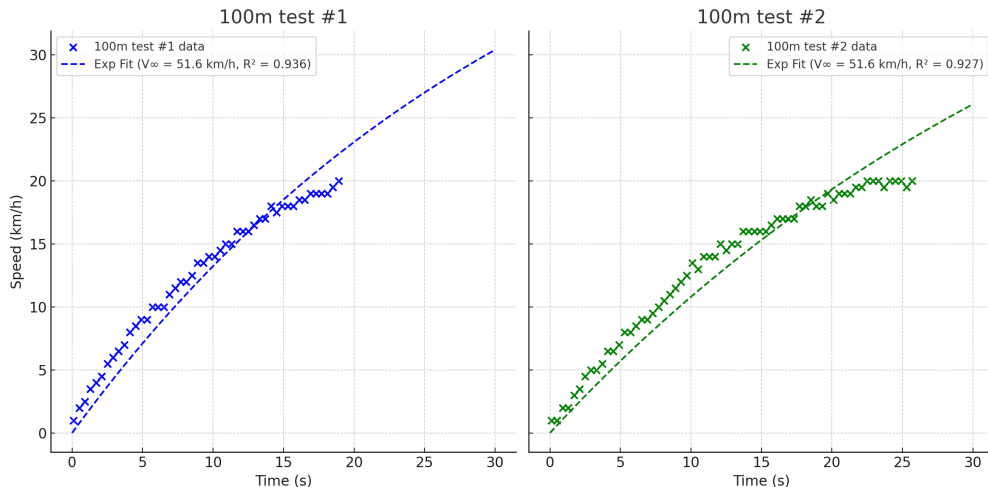


Figure 16: Initial speed trials deprecated after chain snap around 20 km/h, with extrapolations to the speed that could have otherwise been achieved after failure.

This issue was resolved via three additional improvements that maintained the strengths of the drivetrain while mitigating its flaws:

- **Slotted Mounting Plates:** Allowed micro-adjustment of motor tension.
- **Belleville Washers:** Axial compliance to absorb small chain length changes under load.
- **Chain Idler System:** Maintained positive tension under full-load dynamic conditions, allowing for a tighter chain still with the desired flexibility of ± 1 cm at top speed. Figure 17 below shows this mitigation of the chain's deviation from its cyclic path with and without the idler as measured. We used a Vernier Motion Detector (listed uncertainty of resolution size 1mm [14]) to measure the deviation of the bottom length of the chain. By accelerating the chain on a stationary table, we avoided chain derailment during the test and instead quantified the full extent of chain deviation inherent to the system with and without an idler.

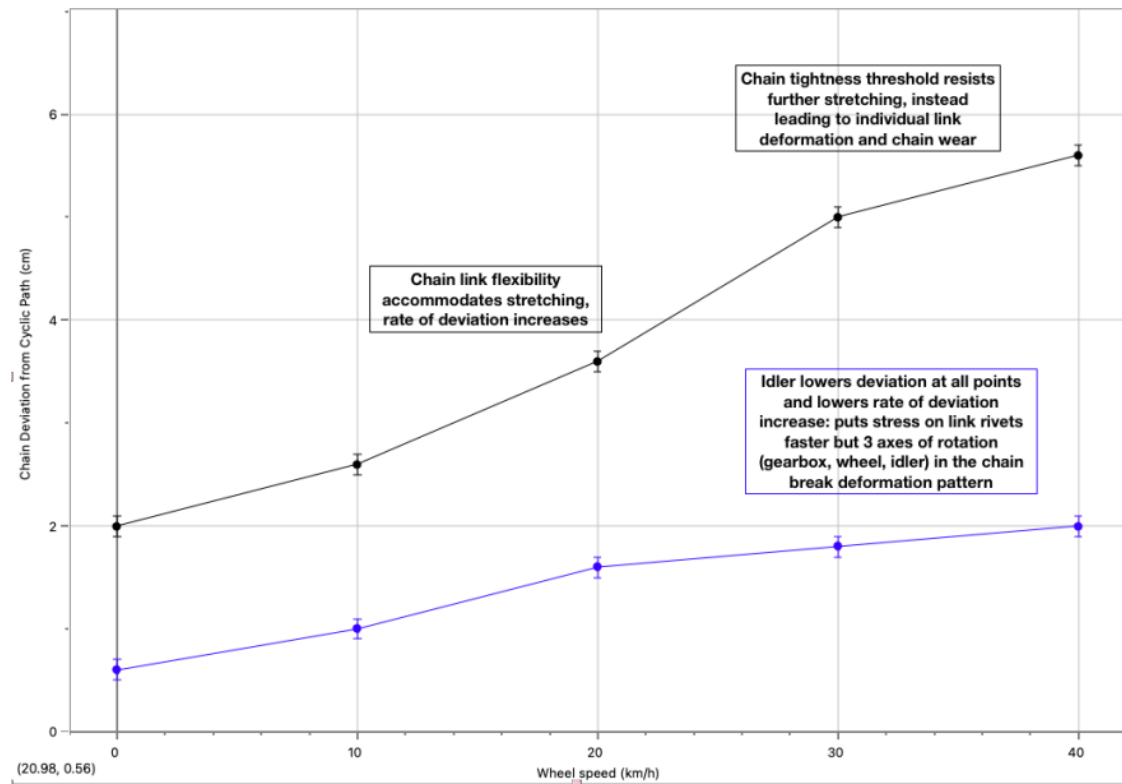


Figure 17: Chain retention improvement after tensioner/idler installation.

While the 0–40 km/h acceleration time remains modest (~ 60 seconds as seen below in Figure 18), this was an intentional trade-off favoring efficiency and cruise performance. Review of race footage and interviews with veteran teams confirmed that the course prioritizes consistent speed rather than rapid stop-start driving, making this optimization both strategic and practical.

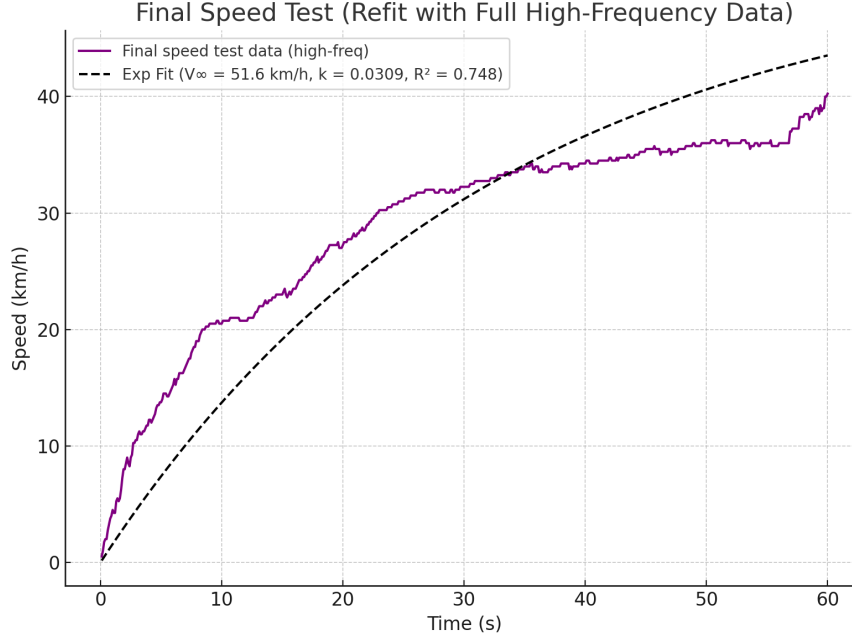


Figure 18: 0-40 km/h acceleration after idler fix (slightly inconsistent acceleration due to track).

6 Electrical System

While our general design philosophy prioritized mechanical simplicity, the electrical system is where complexity was intentionally introduced. This choice was made to increase operational resilience, optimize energy conversion efficiency, and enable quantitative telemetry logging for post-race optimization. This section outlines the design, analysis, and practical justification of each electrical subsystem.

6.1 Power Architecture: 12V to 24V Conversion

The powertrain is based on a 12V Interstate MTX-35 lead-acid battery rated at 55 Ah [15]. Since our selected motor operates at peak efficiency near 24V, we implemented a step-up boost converter with 95% rated efficiency and a 20 A current limit.

$$\begin{aligned}
 P_{\text{in}} &= V_{\text{battery}} \cdot I_{\text{battery}} = 12 \text{ V} \cdot I \\
 P_{\text{out}} &= V_{\text{boost}} \cdot I_{\text{boost}} = 24 \text{ V} \cdot 20 \text{ A} = 480 \text{ W} \\
 \text{Efficiency} &= \eta_{\text{boost}} = \frac{P_{\text{out}}}{P_{\text{in}}} = 0.95 \\
 \Rightarrow I_{\text{battery}} &= \frac{P_{\text{out}}}{\eta \cdot V_{\text{battery}}} = \frac{480}{0.95 \cdot 12} \approx 42.1 \text{ A}
 \end{aligned}$$

At full load, the battery supplies 42.1 A continuously, allowing for an estimated runtime of:

$$t = \frac{55 \text{ Ah}}{42.1 \text{ A}} \approx 1.31 \text{ hours}$$

This calculation was validated through GPS and SD card telemetry, which confirmed that energy depletion and motor temperature profiles closely matched theoretical projections.

6.2 Safety Discharge Subsystem

One potential failure mode in boost-based architectures is a sudden disconnect from the load, which can result in voltage backflow from capacitive components, potentially damaging the converter or motor controller. To mitigate this, we implemented a fail-safe discharge path using a high-wattage resistor, DPDT switch, and a Schottky diode to prevent reverse current draw.

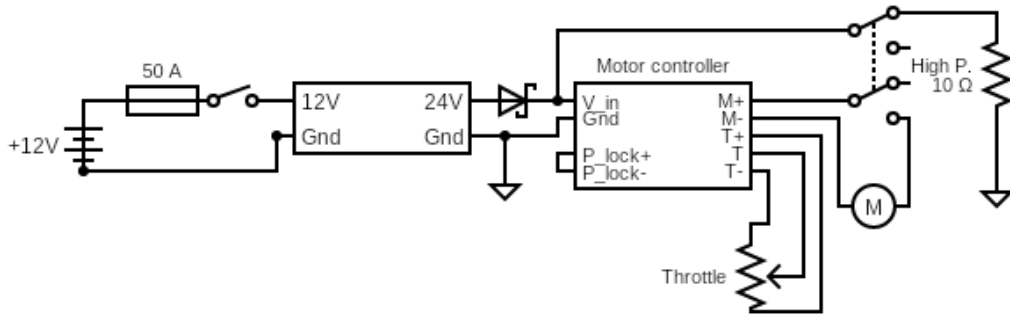


Figure 19: Diagram of the vehicle's electrical system, showing the 12V battery stepped up to 24V via a boost converter, feeding a motor controller with integrated throttle and optional high-power discharge resistor for safe shutdown via a DPDT switch.

- Resistor value selected to dissipate energy from converter capacitors:

$$P = \frac{V^2}{R} = \frac{24^2}{10} = 57.6 \text{ W} \quad (\text{below rated } 100 \text{ W})$$

- Energy stored in capacitors (assuming $2200 \mu\text{F}$ at 24 V):

$$E = \frac{1}{2}CV^2 = \frac{1}{2} \cdot 2.2 \cdot 10^{-3} \cdot 576 = 0.634 \text{ J}$$

- Discharge time constant (RC):

$$\tau = R \cdot C = 10 \cdot 2.2 \cdot 10^{-3} = 0.022 \text{ s}$$

The circuit safely discharges stored energy in < 0.1 seconds after shutoff, avoiding backflow voltage damage.

6.3 Telemetry and Sensing System

Data collection was a key goal, both for performance tuning and engineering analysis. All sensors interface through an ESP32 microcontroller, which streams data to an onboard OLED display and logs it to an SD card.

Measured Quantities and Uncertainties:

- **Wheel Encoder (optical, 360 CPR):** Used to calculate wheel speed and acceleration. At 40 km/h ($\approx 4.56 \text{ rev/s}$), this provides:

$$\text{Ticks/sec} = 4.56 \cdot 360 = 1641.6 \text{ Hz} \Rightarrow \Delta t = 0.61 \text{ ms}$$

This offers precise speed resolution down to $\pm 0.03 \text{ km/h}$.

- **GPS Acceleration/Velocity:** Used to measure course-averaged cruise velocity and verify drivetrain top speed. Time resolution 5 Hz, horizontal precision $\pm 1.5 \text{ m}$, velocity error $\pm 0.1 \text{ m/s}$.
- **Voltage/Current Sensors:** Installed on both sides of the converter to measure:
 - Battery current draw ($\pm 0.2 \text{ A}$, $\pm 0.05 \text{ V}$)
 - Boost converter output current ($\pm 0.1 \text{ A}$)
 - Real-time power tracking:

$$P(t) = V(t) \cdot I(t)$$

The data was processed post-testing in Python to correlate power draw with GPS-measured velocity and evaluate losses across mechanical and electrical subsystems. This enabled us to calculate an observed drivetrain mechanical efficiency of $\sim 70\%$ when compared to our predicted top speeds and acceleration (Table 1), which is close to the theoretical electrical efficiency of 73.9%.

6.4 Thermal Management and Overheating Protection

During early motor controller tests, we observed thermal heating (though no shutdowns) after sustained current draw. The controller case temperature exceeded 60°C . To mitigate this:

- A heatsink was implemented for the motor controller's specific dimensions.
- Thermal paste was used to reduce thermal contact resistance.

Post-upgrade testing showed a sustained controller temperature under 40°C under full load at ambient 25°C , confirming the thermal solution's effectiveness.

7 Concluding Statements

The WOSS Warrig X1 Electrathon vehicle represents a deliberate integration of first principles engineering theory, data-driven decision-making, and robust fabrication. From the implementation of a 3° negative camber angle to optimize lateral grip, to a custom gearbox designed for balance between power and speed, every design choice was validated through simulation, empirical testing, and real-world performance. For our rookie team, the WOSS Warrig X1 vehicle stands as a culmination of successful collaborative engineering effort balancing mechanical performance, energy efficiency, and multi-system innovation under the constraints of limited financial and physical resources. The experience has not only yielded a competitive vehicle but has also strengthened our understanding of mechanical systems, design optimization, and data-driven engineering analysis. We are confident that the WOSS Warrig X1 will serve as both a high-performance entry in competition and a foundation for future innovation at White Oaks Secondary School.

A Appendix A: CAD Drawings

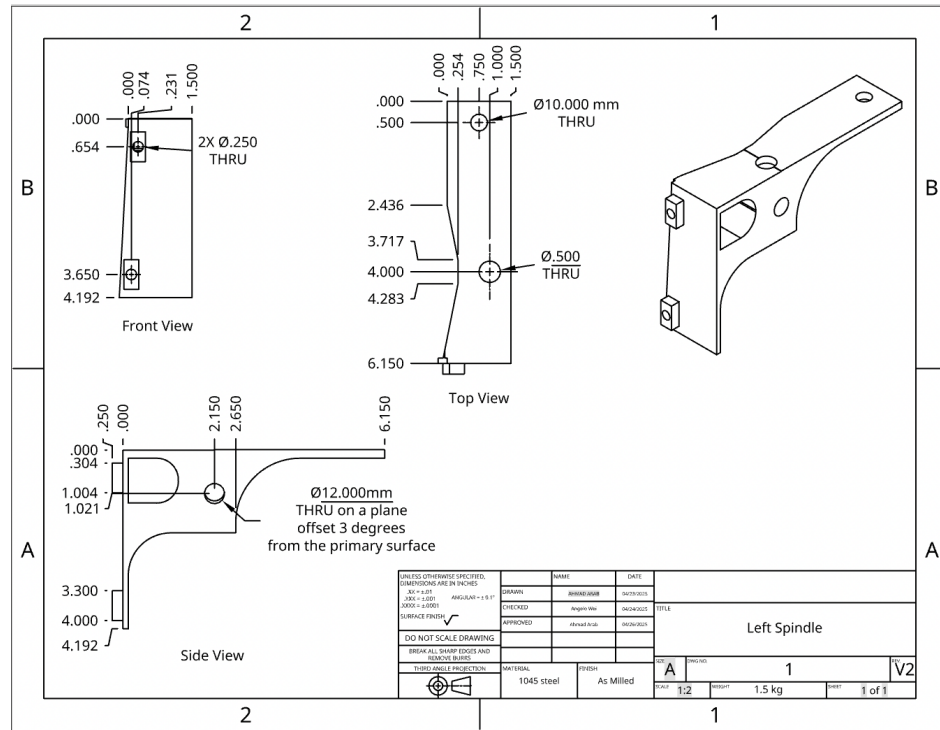


Figure 20: Technical drawing of left spindle, machined on 3-axis CNC.

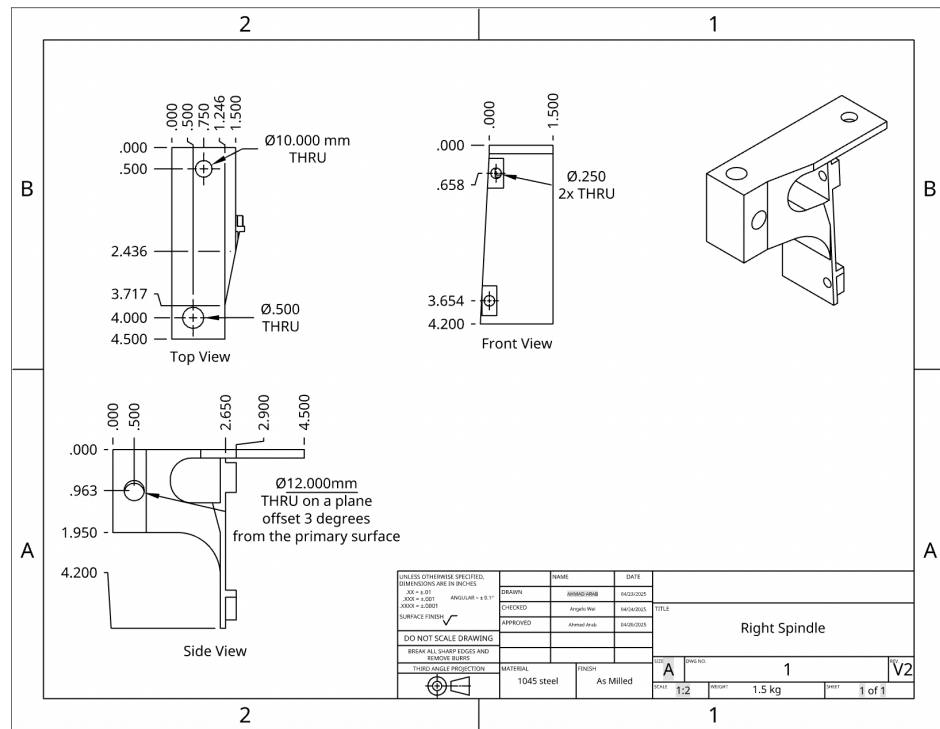


Figure 21: Technical drawing of right spindle, machined on 3-axis CNC.

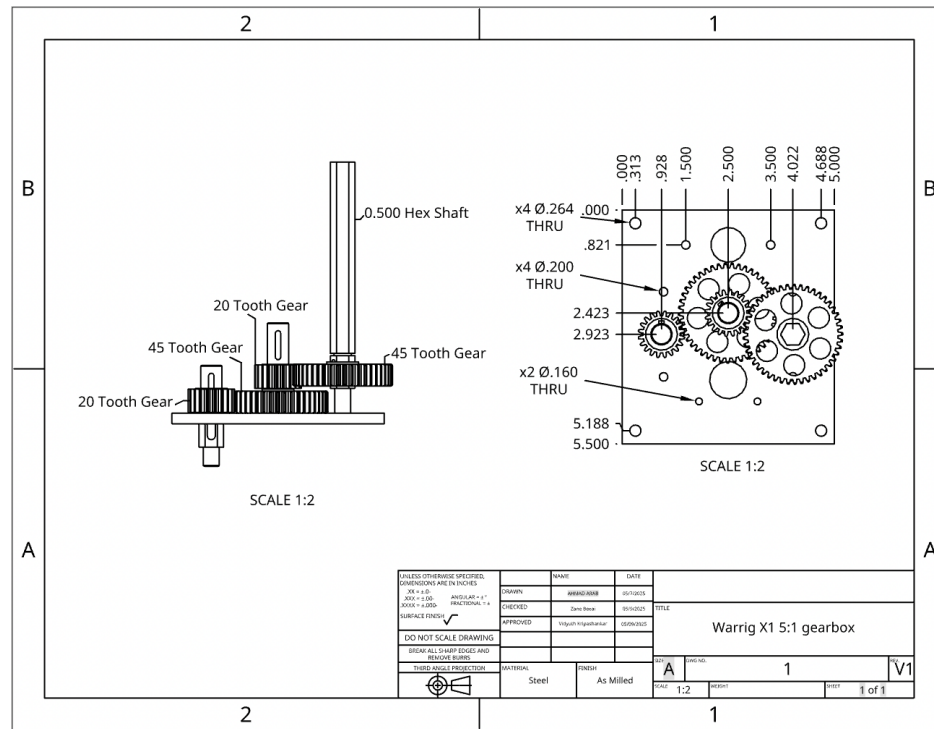


Figure 22: Technical drawing of 81:16 (~5:1) reduction gearbox.

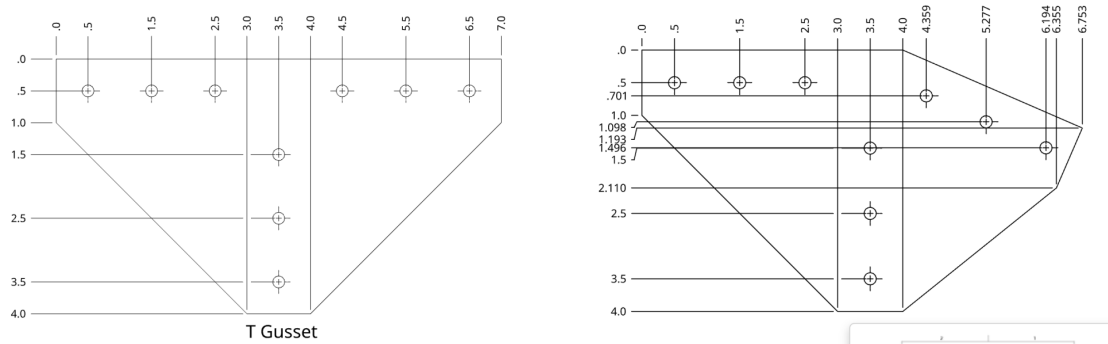


Figure 23: Examples of gussets manufactured and used in the vehicle.

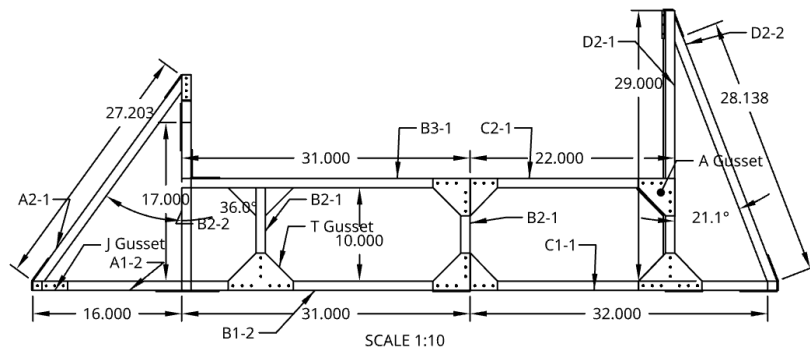


Figure 24: Technical drawing of the Warrig from side orthographic view.

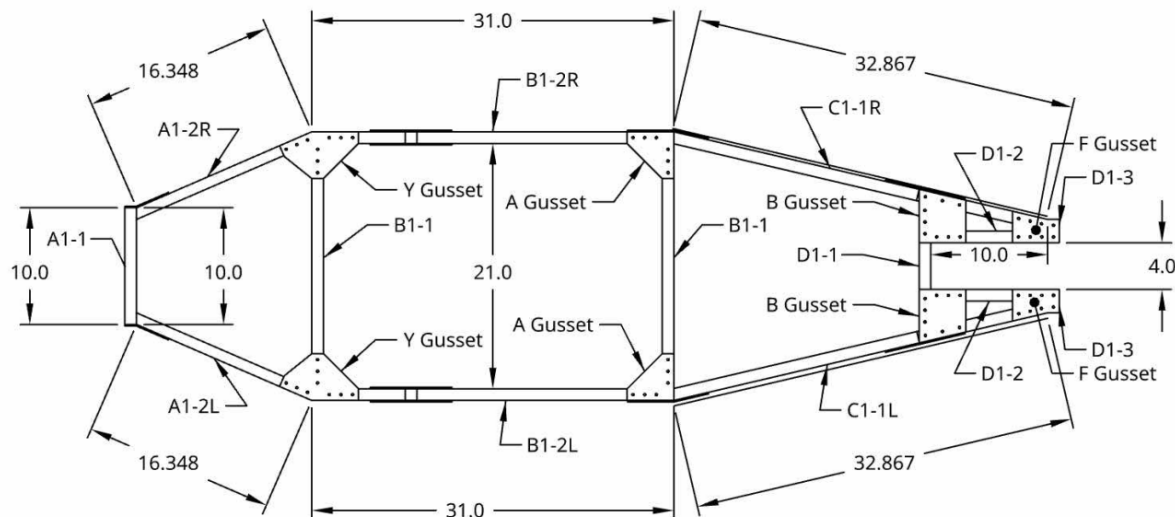


Figure 25: Technical drawing of the Warrig from a floor perspective.

B Appendix B: Data Tables

Component	Weight (lbs)	Distance from Front of Frame (in)
Battery	24	10
Driver	160	57
Motor + Gearbox	15	65
Front Wheel Center	—	17.5
Rear Wheel Center	—	79.5
Back of Frame	—	80

Table 2: Vehicle component weights and positions along the frame.

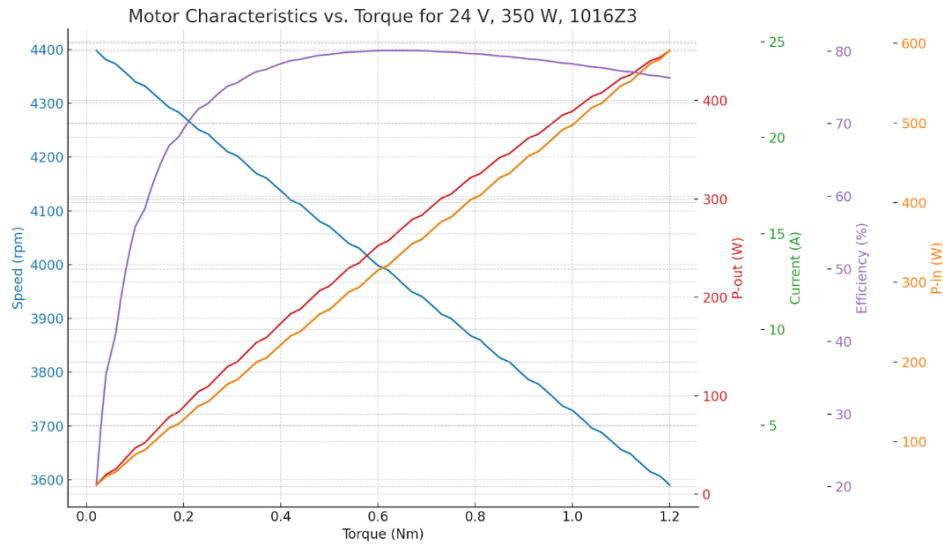


Figure 26: *Incorrect* motor characteristic curve for BY1016Z; data domain is actually internal torque compared to external curve after 9:1 reduction. [11]

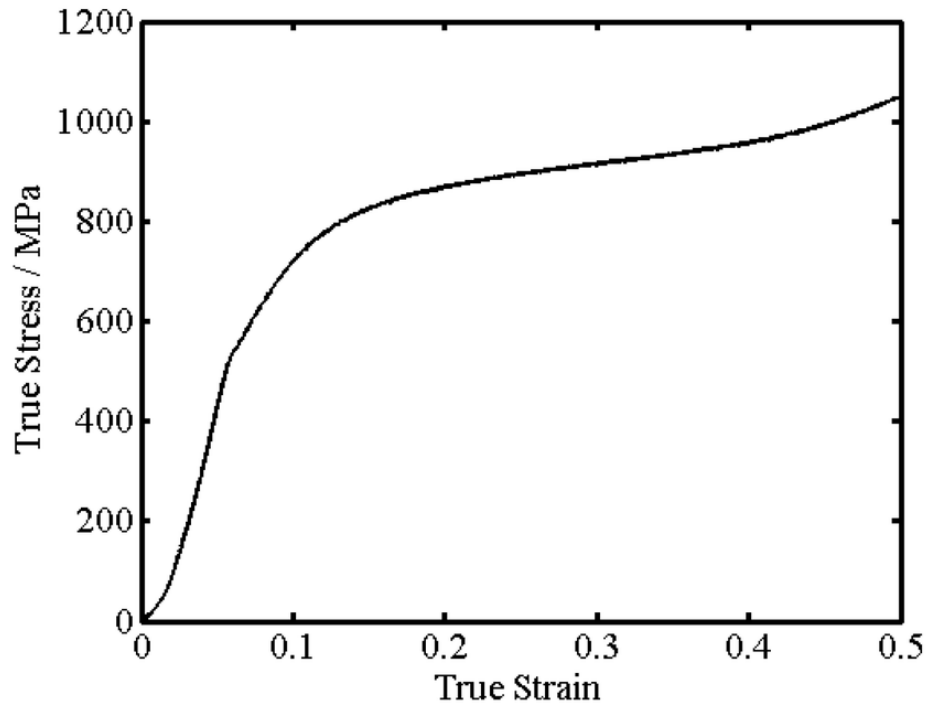


Figure 27: Sample stress-strain curve for 1045 steel. [16]

C Appendix C: Additional Calculations

C.1 Derivation of Linear Acceleration from Torque

We aim to derive the linear acceleration a of a wheel under a given torque τ , wheel diameter d , and load mass m .

By definition, torque is the product of force and radius:

$$\tau = F \cdot r \implies F = \frac{\tau}{r}$$

As the force on the wheel's edge. Using Newton's second law:

$$a = \frac{F}{m}$$

Substitute the expression for F :

$$a = \frac{\tau}{r \cdot m}$$

Wheel radius r is half the diameter. If diameter d is given in inches, convert to meters:

$$r = \frac{d \cdot 0.0254}{2}$$

Substitute r into the acceleration equation:

$$a = \frac{\tau}{\left(\frac{d \cdot 0.0254}{2}\right) \cdot m}$$

$$a = \boxed{\frac{2\tau}{d \cdot 0.0254 \cdot m}}$$

C.2 Uncertainty in Speed Measurement using a 360 CPR Quadrature/Encoder

We are measuring the speed of a wheel with:

- Diameter: $d = 24$ inches
- Encoder Resolution: 360 CPR (Cycles Per Revolution), which gives $360 \times 4 = 1440$ counts/rev in quadrature
- Sampling time: $\Delta t = 0.1$ seconds

$$C = \pi \cdot d = \pi \cdot 24 \approx 75.4 \text{ inches}$$

$$\Delta x = \frac{C}{1440} = \frac{75.4}{1440} \approx 0.05236 \text{ inches/count}$$

where Δx is the linear distance per count, and consolidating speed measurements with intervals of $\Delta t = 0.1$ s;

$$\Delta v = \frac{\Delta x}{\Delta t} = \frac{0.05236}{0.1} = 0.5236 \text{ in/s}$$

Finally, we convert to km/h to yield:

$$1 \text{ inch} = 0.0254 \text{ meters}, \quad 1 \text{ m/s} = 3.6 \text{ km/h}$$

$$\Delta v = 0.5236 \cdot 0.0254 = 0.0133 \text{ m/s}$$

$$\Delta v = 0.0133 \cdot 3.6 \approx \boxed{0.048 \text{ km/h}}$$

References

- [1] Thyssenkrupp, 2025, accessed: 2025-05-20. [Online]. Available: <https://www.thyssenkrupp-materials.co.uk/density-of-aluminium.html>
- [2] AmesWeb, 2025, accessed: 2025-05-20. [Online]. Available: https://amesweb.info/Materials/Density_of_Steel.aspx
- [3] AZoM, “Aluminum 1060-o - material properties,” 2023, accessed: 2025-05-20. [Online]. Available: <https://www.azom.com/article.aspx?ArticleID=2855>
- [4] “1060-h14 aluminum: Material properties,” 2023, accessed: 2025-05-20. [Online]. Available: <https://www.makeitfrom.com/material-properties/1060-H14-Aluminum/>
- [5] M. Rokonuzzaman and M. R. I. Faruque, “Stress-strain curve of aluminium 1060 for mechanical characterization,” *ResearchGate*, 2023, accessed: 2025-05-20. [Online]. Available: https://www.researchgate.net/figure/Stress-strain-curve-of-aluminium-1060_fig1_359267613
- [6] , “Driver fatigue,” 2019, accessed: 2025-05-20. [Online]. Available: <https://www.sdcc.ie/en/services/transport/road-safety/advice-and-guidance/driver-fatigue/>
- [7] Z. Guohua, L. Liu, D. Wang, J. Guo, and W. Chen, “Mechanical properties of aisi 1045 steel subjected to combined loads of tension and torsion,” *Experimental Techniques*, Mar 2018.
- [8] R.Santos, “The absolute guide to the racing tyres – part 1: Lateral force,” 2014, accessed: 2025-05-20. [Online]. Available: <https://racingcardynamics.com/racing-tires-lateral-force/>
- [9] D. H. Mike Blundell, “Chapter 5 - tyre characteristics and modelling,” 2015, accessed: 2025-05-20. [Online]. Available: <https://www.sciencedirect.com/science/article/abs/pii/B9780080994253000054>
- [10] J. Vogel, “Tech explained: Ackermann steering geometry,” 2021, accessed: 2025-05-20. [Online]. Available: <https://www.racecar-engineering.com/articles/tech-explained-ackermann-steering-geometry/>
- [11] “Amazon-250w-24v-motor,” 2025, accessed: 2025-05-20. [Online]. Available: <https://www.amazon.ca/VEVOR-Electric-Powerful-Motor-Bike/dp/B0DQNWX79C>
- [12] “Ampflow high performance motors,” 2025, accessed: 2025-05-20. [Online]. Available: <https://www.ampflow.com/motors/highPerformance/threeInch/#high-performance>
- [13] I. Steed, “The importance of getting chain tension right,” 2023, accessed: 2025-05-20. [Online]. Available: <https://steedbikes.com/blogs/news/the-importance-of-getting-chain-tension-right?srsltid=AfmBOoqDfj4tjuMxRzTfEhD4tHYLypiWXkj8nKc9pVRG14ps0U-sMKPZ>
- [14] “Motion detector,” 2025, accessed: 2025-05-20. [Online]. Available: <https://www.vernier.com/product/motion-detector/?srsltid=AfmBOorZOGBXifGMnsm42W0xIBo1O6-cPo4akblcRuQS4gbgowyaaJrF>
- [15] “Mtx-35 battery,” 2025, accessed: 2025-05-20. [Online]. Available: <https://www.interstatebatteries.com/products/mtx-35>
- [16] L. Li, Y. Li, Y. Mingshun, and T. Tong, “Process parameters decision to optimization of cold rolling-beating forming process through experiment and modelling,” *Metals*, vol. 9, 04 2019.